International Journal of Refractory Metals and Hard Materials 132 (2025) 107266

Contents lists available at ScienceDirect

International Journal of Refractory Metals and Hard Materials

journal homepage: www.elsevier.com/locate/IJRMHM

Molybdenum 8wt% rhenium alloy processed by laser powder bed fusion: From powder production to mechanical testing at elevated temperatures

Aurore Leclercq [a], Anna Czech [b], Thibault Mouret [a], Marcin Lis [b], Adriana Wrona [b], Vladimir Brailovski [a,*]

[a] Mechanical Engineering Department, École de Technologie Supérieure, 1100 Notre-Dame Street West, Montreal, Quebec H3C 1K3, Canada
[b] Centre of Powder and Composite Materials, Łukasiewicz Research Network - Institute of Non-Ferrous Metals, 5 Sowińskiego Street, 44-100 Gliwice, Poland

ARTICLE INFO

Keywords:
Laser powder bed fusion
Molybdenum-rhenium alloys
Powder production
Mechanical testing
Elevated temperature tests
Crack-free specimens

ABSTRACT

Molybdenum is highly valued in industry because of its unique properties, especially at high temperatures. Additive manufacturing technologies, particularly laser powder bed fusion (LPBF), are becoming increasingly popular for producing complex shapes at a lower cost as compared to the conventional forming processes. However, printing molybdenum with LPBF presents challenges, especially caused by its hot cracking susceptibility. Several approaches have been explored to address this issue, including alloying molybdenum with other elements, which has proven effective in enhancing the printability and minimizing the occurrence of cracking, particularly with the addition of rhenium. In this study, a combination of mechanical blending of molybdenum powder and a rhenium precursor, followed by the reduction of the precursor and plasma spheroidization, was used to produce spherical 30–55 μm molybdenum-rhenium (8 wt%) powders with rheological properties suitable for LPBF. Compared to pure molybdenum, the use of the alloyed powder led to an increase in the crack-free printed density, from 97 to 98.5 %, and in the compressive strength, from 240 to 340 MPa, at 600 °C and from 150 to 190 MPa at 1000 °C, at the expense of a ~ 5 % reduction in the compression strain. To demonstrate the potential of printing complex geometries using the developed powders, complex geometry artifacts containing 0.25 mm-thin letters, wide dense sections and auto-supported 50 %-density 0.7 mm-thin strut diamond lattice structures were successfully printed.

1. Introduction

Molybdenum (Mo) belongs to the refractory metal group, coming in fourth in line after Tungsten, Rhenium and Tantalum in terms of melting temperature (T = 2896 K / 2623 °C). Like other refractory metals, molybdenum is distinguished by its excellent electrical [1] and thermal [2] conductivity, a low coefficient of thermal expansion [3], as well as a high mechanical [4], wear [5] and corrosion [6] resistance. This element is regularly introduced in small concentrations into the compositions of advanced alloys (e.g., various INCONEL®, Hastelloy B or titanium alloys, such as Ti6246 for example) to improve their corrosion resistance. For elevated temperature applications, with UTS = 210 MPa [4] and E = 280 GPa [7] at 800 °C, molybdenum manifests the highest strength- and stiffness-to-density ratios among all the refractory metals. Due to this unique combination of properties, molybdenum is a promising candidate for various applications in different fields, including the medical, petrochemical, aerospace and defense industries [8,9].

The creation of semi-finished molybdenum products (e.g., sheets, rods and bars) is currently driven by conventional forming processes, mainly including powder metallurgy and plastic deformation processes, such as forging, rolling, etc. To manufacture complex geometries, subtractive and joining processes are required, but these have their own limitations when applied to refractory metals, such as high machining costs and a strong oxygen affinity in the heat affected zone. In response, the recent and rapid development of additive manufacturing (AM) technologies offers a promising technical solution enabling the production of complex shapes at reduced processing cost. Over the years, numerous AM technologies have been tested to print refractory metals [10,11], each with its own pros and cons. The layer-by-layer laser powder bed fusion (LPBF) is the most mature AM technology. The process uses a laser heat source to sequentially melt one layer of powder at a time according to a pre-defined pattern generated from a sliced 3D

* Corresponding author.
E-mail addresses: aurore.leclercq.1@ens.etsmtl.ca (A. Leclercq), Anna.Czech@imn.lukasiewicz.gov.pl (A. Czech), thibault.mouret@etsmtl.ca (T. Mouret), Marcin.Lis@imn.lukasiewicz.gov.pl (M. Lis), Adriana.Wrona@imn.lukasiewicz.gov.pl (A. Wrona), vladimir.brailovski@etsmtl.ca (V. Brailovski).

https://doi.org/10.1016/j.ijrmhm.2025.107266
Received 17 April 2025; Received in revised form 26 May 2025; Accepted 27 May 2025
Available online 29 May 2025

CAD model of the desired part. In contrast to its main competitor, electron beam powder bed fusion (EB-PBF), LPBF is distinguished by its higher resolution, greater printing flexibility, and lower processing costs [12,13].

Notwithstanding all the advancements in industrial LPBF application, the printability of molybdenum remains a significant challenge. The high energy input required to reach the melting temperature and the rapid solidification rate of the process result in substantial temperature gradients and residual stresses. Additionally, the high ductile to brittle transition temperature (DBTT) of molybdenum contributes to its susceptibility to cracking during printing. The DBTT of molybdenum is reported to be highly dependent on the segregation of impurities at the grain boundaries (GB) and on the material microstructure [14–17]. Most researchers agree to consider molybdenum as a crack-prone material, and many of them tried to overcome this problem using different strategies including optimization of printing parameters [10], preheating of the baseplate [18–20], and preheating of the powder bed using a multiple exposure approach. To date, the two first strategies have demonstrated low-to-zero efficiency, while the third approach has appeared to be more technologically promising but less economically efficient in this regard [21].

In the literature, alloying molybdenum with different elements represents a common solution for improving its printability, increasing its density, and simultaneously, mitigating hot cracking [22–26]. Various alloy compositions have been tested, and depending on the nature of the alloying elements involved, several types of microstructural modifications improving the cracking resistance of molybdenum have been reported. These modifications target the main factors responsible for cracking, including the propensity to form irregular microstructures or to segregate interstitial elements at grain boundaries (GB). In fact, alloying has been successfully used to transform coarse columnar microstructures into equiaxed grain structures or submicron cell structures [23,27,28]. Alloying has been also successfully used to promote GB cohesion and to limit their oxidation [24,25], as well as to decrease the DBTT [29,30]. Thus, depending on the physical, mechanical and microstructural features expected, the selection of alloying elements is fundamental. Moreover, both the pre-alloyed powders and in-process alloyed powders can also be considered in this regard.

As an example, dispersion within the powder bed of oxygen-sensitive elements, such as carbon (C, 0.45 wt%, [23]) under its elemental form, or through the use of silicon carbide (SiC, 0.1 wt%, [24]), appeared to be a promising solution to increase the printed density of molybdenum and to reduce its brittleness. In the atmospheric conditions of the LPBF process (O_2 low partial pressure), these species enable the reduction of the overall oxygen content, through the outgassing of a volatile carbon monoxide CO. Thus, segregation at the grain boundaries and the formation of detrimental molybdenum oxide MoO_3 is limited. Furthermore, elemental carbon powders modify the solidification behavior and lead to a refined cellular microstructure, with molybdenum surrounded by molybdenum carbide Mo_2C, while nanosized SiC particles apparently block dislocations and inhibit the propagation of cracks. Effectively, by combining the dispersion of elemental carbon powders with the baseplate preheating to up to 800 °C, the authors of the referenced studies were able to reduce cracking.

Alloying refractory metals with others transition metals was also found to be effective in inhibiting the cracks formation associated with the LBPF process by Gan et al. [25] who successfully used chromium (Cr) and titanium (Ti) additions into molybdenum. For their part, Guo et al. [28] dispersed nickel (Ni) and iron (Fe) nanoparticles within tungsten powders. In both cases, the authors reported cracks suppression. From their observations, using nanosized particles with a large surface area promote the formation of an equiaxed fine grain microstructure with sufficient ductility to prevent cracking. Conversely, with coarser particles (μm range), they attributed the resistance to cracking to the formation of solid solutions strengthening the parts and capturing oxidation traces (MoO_3) in the melt pool. Recently, some authors have also steered their attention to high-entropy refractory alloys (RHEA) [31,32].

One of the most common and commercially available Mo alloys is Titanium-Zirconium-Molybdenum (TZM). It contains small concentrations (<1 wt%) of titanium, zirconium and carbon enhancing its mechanical strength through the precipitation of Mo and Ti carbides. This mechanism is analogous to the process observed with the addition of elemental carbon powders. In fact, oxidation, carboreduction and outgassing inhibit segregation of impurities at the grain boundaries through the formation of gaseous carbon monoxide and titanium oxides (TiO bp = 3227 °C, TiO_2 bp = 2970 °C) [33]. The same authors also reported oxygen bounding with zirconium (ZrO_2) and with $(Mo,Ti)_xC_y$ precipitates, which lead to LPBF parts with purified grain boundaries. They also demonstrated that a TZM-modified alloy with an increased carbon content (up to 2.3 at.%) enables to create refined and isotropic cellular microstructures with improved elevated-temperature mechanical properties (YS = 450 MPa, UTS = 600 MPa at 800 °C) over what could be obtained using conventional processes [34]. In all cases, the authors of the above works reported the LPBF production of high density and crack-free TZM samples. The main drawback of the TZM alloy is its high price per weight ratio, which is at least three times higher than that of pure molybdenum. This is the reason why the most common alloying solution for refractory metals continues to be their combination in dual alloys with reduced DBTT, enhanced ductility, and suppressed cracking [35–37].

In the above context, rhenium (Re) represents one of the most promising alloying elements for dual refractory alloys, notwithstanding a related increase in powder cost. For example, alloys such as Mo47.5Re or W25Re30Mo (wt%) have shown remarkable enhancements in their mechanical properties at room [35] and high [38] temperatures, respectively. Oehlerking et al. [26] reported the successful LPBF printing of complex demo parts with Mo47.5Re powders and an almost 60 % improvement in their room-temperature mechanical properties. However, the authors were not able to prevent cracking due to an excessive residual oxygen content. Eckley et al. [39] investigated the impact of adding 5, 10 and 25 wt% of rhenium on the room-temperature flexural strength of Mo—Re alloys. They reported a softening effect occurring for the low Re content, no changes for the intermediate Re content, and a slight hardening for the high Re content. These results are in agreement with the extensive study conducted by J. Stephens and W. R. Witzke [40], who identified a Re threshold separating the softening and the hardening behavior of Mo—Re compounds at Re ≈ 16 at.% and/or at $0.16T_m$ Mo (~420 °C).

Although the production catalogues of powder manufacturers have grown significantly over the years, the process of obtaining molybdenum-based powders with specific alloying compositions, such as those described previously, remains challenging and costly. The powder production step is crucial as the quality of LPBF parts is significantly influenced by the uniformity and density of the powder bed, which in turn depends on the morphology and size distributions of powder particles [41,42]. Traditional mechanical methods (e.g., grinding, mechanical synthesis, etc.) or physicochemical methods (e.g., reduction of compounds, condensation from the gas phase, synthesis from solutions, etc.) used to produce alloyed powders are unsuitable for this process. Powders produced with such methods are generally characterized by an irregular particle shape and a low bulk density, likely to negatively affect the density and mechanical properties of printed parts.

Spherical powders can be produced using different physical atomization methods. Wide applications of some of these methods, such as the plasma rotating electrode process (PREP) [43–45] or ultrasonic vibrations-assisted atomization [46,47], are limited because of the accompanying low production rates. The use of other physical methods, such as water atomization, is much more cost-effective, but results in somewhat coarse and irregular-shape particles. Moreover, the high oxygen intake inherent to this process makes it incompatible with reactive metals such as titanium or aluminum [48] and unsuitable for refractory

metals which are also highly sensitive to oxygen content. The gas atomization method, while being largely used for the production of metal powders for 3D printing [49,50], has limited applicability for refractory metals because of their extremely high melting temperatures.

To overcome the above difficulties related to the production of refractory powders with a high degree of purity and sphericity, industry principally uses plasma-based techniques, such as plasma atomization and plasma spheroidization [58,59]. In the former case, the feedstock is generally a wire, while in the latter, it consists of crushed powder particles. The use of a wire feedstock requires several resource-intensive steps, involving rolling and drawing, which result in extremely expensive products and carries a significant environmental footprint. For its part, the use of plasma spheroidization is less restrictive, since the technique produces spherical powders from their irregular precursors, the latter obtained by various mechanical (crashing, milling), and therefore, less expensive and less polluting methods. In both cases, however, an ingot of a given alloy composition must be cast, making the production of powders of different target formulations economically challenging. To overcome this, alloyed powders suitable for 3D printing can be produced via chemical modifications of their elementary precursors [51,52] and then subjected to plasma spheroidization.

This study delineates the methodology employed to produce LPBF-ready molybdenum alloy powders containing a low amount of rhenium, Mo8wt%Re, abbreviated as Mo8Re. The alloyed powder is subsequently characterized in terms of its physical and rheological properties and used in a comprehensive printability study involving the physical and microstructural analyses of specimens produced using different combinations of printing parameters. Two optimized sets of printing parameters found during this study are then used to produce specimens for mechanical testing in a wide temperature range. Finally, the results obtained with Mo8Re powders are compared to those acquired with ≥99.9 %Mo powders, to reveal the effect of a relatively limited rhenium addition on the LPBF printability and mechanical properties of molybdenum.

2. Materials and methods

2.1. Powder production

Two powder lots were concurrently used in the context of this study: the first is a commercial (Tekna Co. Ltd., Sherbrooke, Canada) plasma-atomized molybdenum powder (99.9 % Mo) with the following powder size distribution: D10 = 12.6, D50 = 20.6 and D90 = 32.0 (μm). This powder was considered as a reference feedstock for the LPBF process. The second is an alloyed Mo8Re powder developed for this study.

The production of Mo8Re powders was divided in three successive steps and was entirely realized at the Institute of Non-Ferrous Metal (Łukasiewicz Research Network, Poland). First, the preparation of a feedstock started with the mechanical blending of the molybdenum powder and the rhenium precursor, followed by the latter being reduced to obtain a Mo—Re mixture. To this end, commercial high purity Mo powder (99.99 %, KAMB Import Export) with a particle size range of 17–78 μm was selected. Regarding the rhenium, it was introduced as ammonium perrhenate (APR) NH_4ReO_4 (99.9 %, Innovator Ltd). The mixture was made according to the stoichiometric Mo8Re proportions (88.87 %wt Mo + 11.52 %wt NH_4ReO_4). The reduction process that enables to obtain metallic rhenium was conducted at 800 °C in 100 % hydrogen atmosphere for two hours. This specific temperature is associated with the APR reduction temperature. During the thermal treatment, direct NH_4ReO_4 reduction (1) and/or indirect reduction from the oxides (mainly Re_2O_7, ReO_3 and ReO_2) occur, depending on the temperature of the reaction [53].

$$2NH_4ReO_{4(s)} + 7H_{2(g)} = 2Re_{(s)} + 8H_2O_{(g)} + 2NH_{3(g)} \quad (1)$$

Then, the Mo—Re mixture was introduced in a customized plasma spheroidization system. To generate Ar—H_2 plasma, a 7 MB plasma torch was used (Sulzer Metco [54]). The addition of hydrogen enables to increase the enthalpy and temperature of plasma flame, which is beneficial in the production of spherical high-melting powders. The powder was injected perpendicularly into the plasma flame area, melted inside and sprayed in the form of spherical droplets. After leaving the plasma zone, liquid particles were rapidly cooled down in an inert atmosphere to minimize their oxidation. The plasma spheroidization parameters used are summarized in Table 1. This spheroidization step is an essential stage of the whole powder production technology chain. It enables to improve the flowability of powder by changing the particle morphology from irregular to spheroidal, also enhancing the overall chemical composition homogeneity and bulk density.

The literature demonstrated that the presence of oxygen in powders and printed parts made of molybdenum is one of the main factors leading to embrittlement and cracking during the LPBF process. Consequently, to minimize the oxygen content, a supplementary deoxidization process of the spheroidal powder was conducted at 1050 °C for one hour in a 100 % hydrogen atmosphere. A final sieving step through a 90 μm sieve was realized before the powder was used for LPBF printing.

2.2. Powder characterization

2.2.1. Chemical and phase analyses

The element distribution within the powder was assessed using an electron probe microanalyzer (EPMA) (JEOL JXA-8230, JEOL Ltd., Japan) and its EDS detector. The oxygen content in the powder was obtained with an IR spectroscope (LECO ON836, LECO Corp., USA). The crystalline structure of the powder was determined by X-ray diffraction (XRD) (Seifert XRD7, Cu source, GE Inspection Technologies, USA). These observations and analyses were conducted at different stages of the process to evaluate the efficiency of the production steps.

2.2.2. Physical and rheological analyses

The particle size distribution (PSD) was measured using an Analysette 22 Nanotec powder size analyzer (Fritsch, Germany), while its pycnometric density was obtained using an Accupyc 1340 helium pycnometer (Micromeritics, USA). The efficiency of the spheroidization step was evaluated by measuring the specific surface area, using the BET method (Gemini 2360, Micromeritics, USA). The powder flowability was measured using a Hall flowmeter according to the ISO 4490-2018 standard (50 g). Additional rheological measurements were carried out using an FT4 powder rheometer (Freeman Technology, UK). This equipment possesses different testing modes for which detailed information and listed outputs can be found in the manufacturer's documentation and publications [55,56]. The rheological behavior of the produced Mo8Re powder was compared to that of a pure molybdenum powder used in the reference work [57]. Five testing modes were applied, namely dynamic flow, aeration, permeability, compressibility and shear. Table 2 summarizes the metrics obtained from these tests.

Finally, the Additive Manufacturing Suitability (*AMS*) figure of merit (2) was used to express the overall suitability of two powder lots for LPBF. The figure was first defined in a work dedicated to the comparison of Ti-6Al-4 V powders [58] and aims to compare different powder lots of the same material based of selected rheological characteristics representative of the LPBF process. The smaller the *AMS* value, the more suitable the selected powder for the LPBF process:

Table 1
Plasma spheroidization process parameters.

Current (A)	Plasma gas flow rate-argon (l/min)	Plasma gas flow rate-hydrogen (l/min)	Carrier gas flow rate-argon (l/min)	Powder feeder plate revolutions (rpm)
500	50	10	4	2

Table 2
List of metrics extracted from the rheometer FT4 analysis and their subsequent influence on the powder flowability.

Testing mode	Metrics	Interpretation
Dynamic flow	Basic Flow Energy (*BFE*, mJ)	Represents the resistance to flow in confined environment
	Specific Energy (*SE*, mJ/g)	Indicates how powder will flow in an unconfined environment and provides an indication about the shear forces acting between particles
	Bulk Density (*BD*, g/cm^3)	Represents the bulk density of the conditioned powder
	Flow Rate Index (*FRI*, w. u.)	Represents the sensitivity of the powder to flow rate change
Aeration	Aeration Energy at 10 mm/s air speed (AE_{10}, mJ)	Traduces the sensitivity to aeration
	Aeration Ratio (*AR*, w. u.)	
Compressibility	Compressibility Index (*CI*, %)	Measures the ability of the powder to become compacted when subjected to normal stresses (Packing ability)
Permeability	Pressure Drop (*PD*, mbar)	Measures the ease with which the powder will release air over a range of stress conditions
Shear	Cohesion coefficient (*CC*, kPa)	Represents the powder internal resistance to flow
	Flow Function (*FF*, w. u.)	Measures the shear stress required to initiate flow in a consolidated powder

$$AMS = \frac{\frac{1}{\rho_{powder}} + CI + PD + SE + AE_{10} + BFE + CC}{7} \quad (2)$$

where ρ_{powder} is the relative powder bed density obtained from (3).

$$\rho_{powder} = \frac{BD}{\rho_s} \quad (3)$$

where ρ_s is the material density obtained by the pycnometer measurements of each powder lot.

2.3. LPBF process and plan of experiment

In the literature, various printing parameter sets have been tested in a bid to improve the printability of pure molybdenum, leading to very divergent results due to the impact of multiple phenomena occurring during printing (lack of fusion, cracking, etc.). However, a critical analysis of the results obtained in a previous study using a 200 W-power LPBF printer [57] enabled to highlight general trends and formulate some potential solutions to solve the above problems. These solutions include the reduction of the scanning speed and the optimization of the hatching space for a given laser spot size. That was carried out using a series of printing parameter sets defined in the volumetric energy density (*VED*, (4)) - build rate (*BR*, (5)) coordinates:

$$VED\ [J/mm^3] = \frac{P}{vht} \quad (4)$$

$$BR\ [cm^3/h] = vht \quad (5)$$

where P (W) is the laser power; v (mm/s), the scanning speed; h (µm), the hatching space and t (µm), the layer thickness.

For pure molybdenum, two different *VED-BR* sets provided superior results in terms of the printed density and the mechanical properties at room and elevated temperatures: 750 J/mm^3–0.86 cm^3/h and 400 J/mm^3–1.62 cm^3/h. Consequently, the same two *VED-BR* sets, herein called Set I and Set II (analogous to the *VED-BR* combinations C and in E in the reference study [57]), were considered in the present study for Mo8Re printing. To optimize the printing parameters using these *VED-BR* combinations, the hatching space value was incrementally increased (h = 40, 60, 80, 100 and 120 µm) to cover the 1.1 to 4 h/t ratio range. The printed samples were tagged with their respective *VED-BR* set and hatching space denominations. For example, specimen I-80 stands for the one obtained with *VED* = 750 J/mm^3, *BR* = 0.86 cm^3/h, i.e., laser power P = 179 W, scanning speed v = 100 mm/s and hatching space h = 80 µm. Note that the layer thickness t was constant and equal to 30 µm in all the cases. Table 3 summarizes the printing conditions of the experimental plan.

The Mo8Re powders were printed under argon atmosphere on a Trumpf Truprint1000 system with a 200 W dual laser source. The printing parameters described in the plan of experiments above were used to produce ten cylindrical specimens (h = 20 mm, Φ = 10 mm), with 5 mm-thickness dense supports (Fig. 1a). All the specimens were printed on a stainless-steel baseplate without preheating. After removal from the baseplate, the specimens were cut and the samples obtained were used for structural analyses and compression testing at room temperature, RT (Fig. 1a). Based on the printed density values measured and on the results of the RT testing, one parameter set was selected as being the best, and it was then used to print specimens for compression testing at elevated temperatures (600, 800 and 1000 °C).

In addition to the cylindrical specimens used to optimize the printing parameters, lattice-containing artifacts in the shape of a pineapple were produced (Fig. 1b). Apart from the aesthetic aspect, this complex geometry part contains some design features which are challenging to print with the LPBF process, such as thin walls, fine letters, wide dense sections and self-supported structures.

2.4. Density measurements

The densities of the printed samples reported in the study were evaluated using the image analysis method. Their z-y cross sections were mounted in carbon-doped resin and mirror-polished and subjected to microscopic observations using a LEXT OLS4100 (Lext Olympus Corp., Japan) laser confocal microscope. The raw images were binarized in the MATLAB environment (R2022b, MathWorks, USA), considering a local grey level threshold adjusted to the mean intensity of vicinity pixels. The overall level of porosity was quantified using the white-to-black pixels ratio. The image analysis was carried out on three different observation areas, representing a major part of the samples' cross-sections (~40 mm^2). The same images were also used to calculate the pore density (pore/mm^2), size (equivalent diameter *DE* in µm, (6)) and shape (circularity *C* without unit, (7)). To focus on the most impactful pores (from a mechanical property viewpoint), while considering limitations related to the measurement resolution (1 px = 2.5 µm), all the pores smaller than *DE* = 20 µm were removed from the analysis. Of note, the contribution of these pores to the overall porosity was negligible, since

Table 3
Variations of the two parameters sets (I and II) printed with a layer thickness of 30 µm.

Set	Name	Hatching Space (µm)	Power (W)	Speed (mm/s)	Volumetric Energy Density (J/mm^3)	Build Rate (cm^3/h)
I	I-40	40	179	199	750	0.86
	I-60	60		133		
	I-80	80		100		
	I-100	100		80		
	I-120	120		66		
II	II-40	40	180	375	400	1.62
	II-60	60		250		
	II-80	80		188		
	II-100	100		150		
	II-120	120		125		

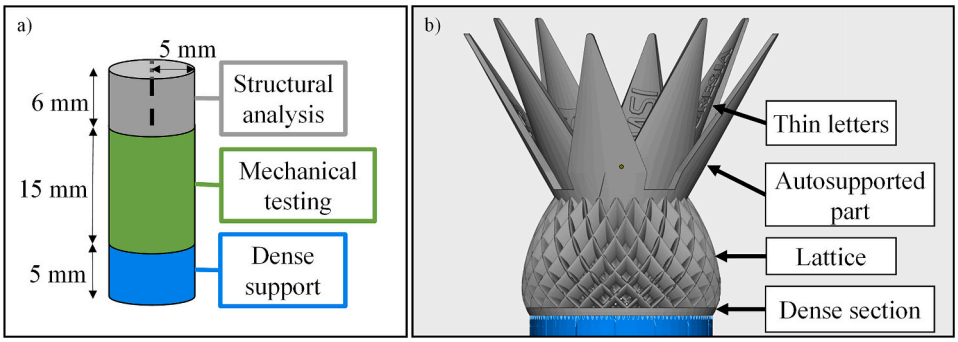

Fig. 1. a) Schematic representation of a printed specimen with samples for structural analyses and mechanical testing; b) Pineapple artifact with design features.

they represented only ~5 % in terms of the cumulative pore surface area.

$$Equivalent\ Diameter\ (DE) = \sqrt{\frac{4Area}{\pi}} \tag{6}$$

$$Circularity\ (C) = \frac{4\pi Area}{Perimeter^2} \tag{7}$$

The image-based density measurements were repeated on different cross-sections of the same sample and on different samples printed using identical parameters. These inter- and intra-part measurements demonstrated that the pore distributions in all the printed samples were relatively uniform, with only slight observable variations.

It should be noted that while the 2D image-based measurement technique used in this study provides only local information about process-induced porosity, it nevertheless represents a reasonable choice since no other porosity detection technique was found suitable for printed molybdenum. For example, the high density of molybdenum (ρ = 10.22 g/cm^3) limits the use of X-ray micro-computed tomography with this material. Also, printed density values measured using the Archimedes technique are frequently compromised by the presence of unmelted particles trapped inside the pores [59,60].

2.5. Crystallographic and microstructural analyses

The crystallographic structure of printed samples and traces of their potential oxidation were assessed using X-ray diffraction analysis (X'Pert3, Co source, Malvern Panalytical Ltd. – UK). A deeper investigation of the oxidation of printed parts was realized using an IR spectroscope (LECO ON836, LECO Corp., USA). A WDS analysis using an Electron Probe Microanalyzer (EPMA) (JEOL JXA-8230, JEOL Ltd., Japan) was used to evaluate the Mo/Re composition ratio inside the printed parts.

The microstructural analyses were carried out on the z-y cross-sections of printed samples using a field emission scanning electron microscope (Hitachi SU-8230, Hitachi Ltd., Japan) equipped with an electron backscattered diffraction detector (EBSD) (e$^-$Flash^{HR}, Bruker, USA). Prior to the inspection, the polished mounted surfaces were ion milled with a Hitachi EM 4000 plus system (5 kV, 25 rpm, 15 min). The post-treatment of EBSD maps was carried out using the MATLAB MTEX library. From these maps, the grain size, orientation and distribution were extracted according to the E2627–13 ASTM standard [61]. In the present work, these metrics are described by analogy to the pore description, as the grain density (grain/mm^2), size DE_g (μm) and circularity C_g (without unit). Additional data, such as the band contrast (BC) diagrams and the MacKenzie distributions are also plotted to reveal the presence of substructures and defects. Two subgroups of structural elements are defined depending on the misorientation angle measured, the low angle grain boundaries (LAGB) structural elements, considering the angle range between 2 and 10°, and the high angle grain boundaries (HAGB) structural elements with angles greater than 10°. These substructural elements are quantified using their density values (μm^{-1}) calculated as a ratio of the LAGB and HAGB lengths to the total indexed area.

2.6. Mechanical properties

Room-temperature compression testing of the specimens in their as-built state was realized in conformity with E9–09 ASTM standard [62] using an Alliance RF/200 testing machine (MTS, Eden Prairie, MN, USA) and 0.01 mm/s compression rate. The force applied during testing was measured by a 200 kN MTS load cell and the displacement monitored using an LVDT. From the strain-stress diagrams plotted, the following metrics were extracted: the maximum stress reached during the test (Ultimate Compression Strength, UCS, MPa), the yield stress (Yield Strength, YS, MPa), calculated at 0.2 % on the strain axis, and the strain under maximum load (δ, %). For each testing temperature, three samples were tested. The compression failure mode was monitored and recorded using a camera located in front of the sample.

High temperature compression testing (600, 800 and 1000 °C) was realized on an MTS 810 testing machine (MTS, Eden Prairie, MN, USA), under argon-controlled atmosphere (flow rate of 27.5 ft^3/h). The force applied was measured by a 100 kN MTS load cell and the displacement monitored by an LVDT. The compression rate was set to 0.075 mm/min according to the E209–18 ASTM standard [63]. An infrared furnace, regulated by a K-type thermocouple, was used to control the temperature during the test. Prior to testing, the sample was heated up (stress-free) to the test temperature with a 10 °C/min rate, while monitoring temperature in the core of the sample. This allowed to define a dwell time of 3 min to ensure that the temperature at the sample core corresponded to a preset value. For each testing temperature, three samples were tested. The mechanical properties obtained at room and elevated temperatures were then compared to their best equivalents reported in the previous study on LPBF of pure molybdenum powders [57].

3. Results

3.1. Elaboration and characterization of the Mo8Re powder

3.1.1. Morphological and chemical analyses

Fig. 2 shows SEM images of the alloyed powder at different stages of its preparation. After mechanical blending and APR reduction (Fig. 2a), the feedstock retains an irregular morphology (S_{BET} = 0.4 m^2/g) of the raw molybdenum powder used. Adding rhenium slightly increases the powder density (ρ = 10.5 g/cm^3). The local EDS analysis (Table 4) realized on the particle surface highlighted an excessive amount of rhenium as compared to the targeted composition, meaning that rhenium agglomerated on the Mo particle surfaces during the reduction process. This observation demonstrated that the temperature (800 °C) used was sufficient to reduce the rhenium precursor but too low to homogenize the chemical composition of the powder.

Following the plasma spheroidization process (Fig. 2b), the alloyed

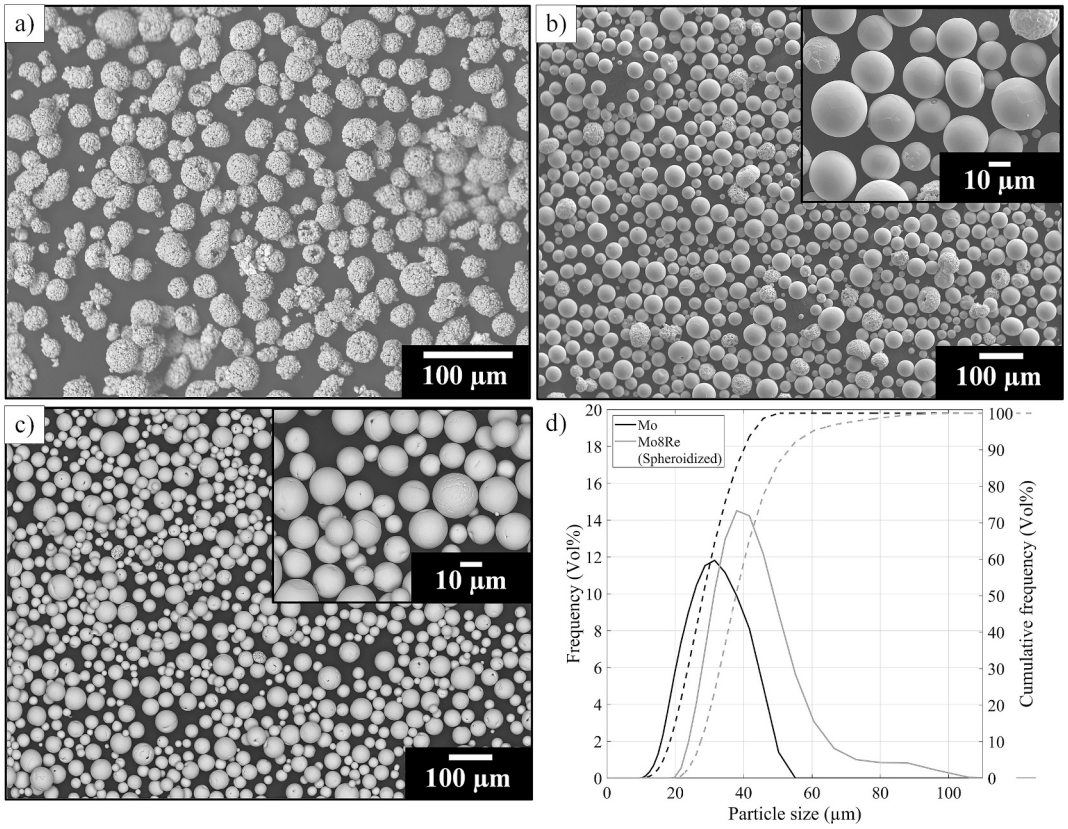

Fig. 2. Scanning electron microscope images: a) Mo8Re powder after mechanical blending, b) Mo8Re after plasma spheroidization, c) Pure Mo used as reference, d) Particle size distributions of both spheroidized powders (Mo8Re and pure Mo).

Table 4
Chemical composition (Mo and Re: EDS, O: IR), morphology and physical properties of the pure and alloyed molybdenum powders.

Powder	Chemical composition (%wt)			Morphology				Physical properties
	Mo	Re	O (ppm)	S_{BET} (m^2/g)	d_{10} (µm)	d_{50} (µm)	d_{90} (µm)	He pycno (g/cm^3)
Mo	99.9*	/	< 500*	/	19.5	29.7	42.1	10.2
Mo-Re Blend	67.1 ± 1.3	32.9 ± 1.3	198	0.4	/			10.5
Mo-Re Spheroidized (round)	92.4 ± 2.5	7.6 ± 2.5	84	0.08	28.7	39.4	55.5	10.5
Mo-Re Spheroidized (satellite)	71.6 ± 16.0	28.4 ± 16.0						

* Commercial data.

powder exhibits the typical spheroidal morphology expected for the LPBF process, resulting in a markedly reduced specific surface (S_{BET} = 0.08 m^2/g). Observations revealed the presence of a limited number of satellite particles having irregular morphologies. However, the powder itself displayed a predominantly circular morphology, much like that of the reference 99.9 % Mo molybdenum powder (Fig. 2c). According to the granulometry measurements (Fig. 2d), the alloyed Mo8Re powder has a slightly larger particle size distribution as compared to its pure molybdenum counterpart.

The EDS analyses realized on the Mo—Re spheroidized powder (Table 4) demonstrate the effectiveness of this step in enhancing the homogeneity of the chemical composition. The reported rhenium content is significantly lower and closer to the targeted proportion (~8 % wt), than in the Mo—Re blend, proving that rhenium which was initially concentrated on the surface is now distributed throughout the volume of the molybdenum particles. This observation is supported by the XRD diffractograms (Fig. 3) and the crystalline patterns identified at each step. After blending, two crystalline structures (Mo, bcc, ICDD 00–042-1120); Re, hcp, ICDD 00–005-0702) are detected, while after the spheroidizing step, only the cubic structure of molybdenum is indexed. According to the Mo—Re phase diagram [64], such a reduced amount of rhenium can be accommodated inside the molybdenum crystalline lattice and form a solid solution. Note that introducing a larger element (such as rhenium) inside the molybdenum cubic structure reduces the interplanar distance and induces a slight shift towards larger angles, as observed in Fig. 3. A simple comparison of this displacement was made with the only $Mo_{0.92}Re_{0.08}$ crystallographic reference available (ICDD 04–001-9280), and suggests a slightly reduced rhenium content compared to the expected composition (8 %wt). No further qualitative estimation through the Rietveld refinement was performed. Moreover, irregular satellite particles retained an excessive amount of rhenium on their surface. The standard deviation obtained for the EDS measurements made on these particles is significant, highlighting the lack of homogeneity of these satellites. According to these observations, the satellite particles were probably not entirely melted by the flame, meaning that the plasma spheroidization process parameters described in Table 1 can still be optimized.

Regarding the final oxygen reduction step, the infrared spectroscopy measurements reaching below 100 ppm (Table 4), indicate a significant decrease in the residual oxygen content. This is beneficial for preventing the oxygen segregation issues at the GB, which are frequently reported for refractories.

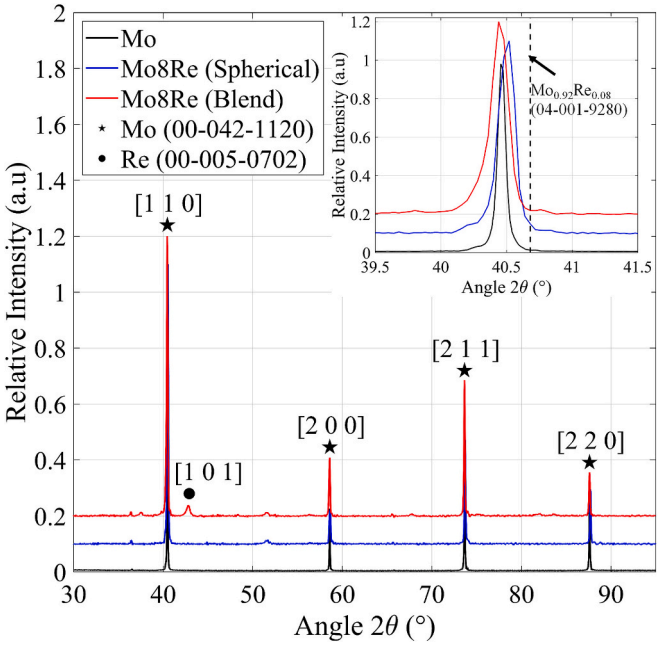

Fig. 3. XRD diffractograms of the alloyed powder at different steps of the process and of pure molybdenum used for the reference study [57].

3.1.2. Flowability and suitability for the LPBF process

The of powder flowability measurements using a Hall flowmeter funnel demonstrate the benefits of the spheroidization process as it divides the required flow time (50 g) by two, between the blended and the spheroidized powders (Table 5). The Hall measurement results of both spheroidized powders, pure Mo and alloyed Mo8Re, are in the same order of magnitude.

The rheological testing made with a FT4 rheometer demonstrates that overall, the two powders are non-cohesive (Table 5). The aeration tests and the resulting elevated aeration ratio ($AR > 20$) show that air easily breaks the weak cohesive forces between the particles. This behavior is corroborated by the cohesive coefficient (*CC*) obtained with the shear tests, which is close to or less than 1. Note that the comparison of these metrics for the two powders highlights that the alloyed Mo8Re powder ($AR = 45$, $CC = 1.3$) is more cohesive than its Mo competitor ($AR = 102$, $CC = 0.33$). The flow function (*FF*) values measured during the shear tests, reinforce this conclusion, since this value is greater for pure Mo powder ($FF = 12.5$, i.e., the free-flowing powder category) than for the alloyed Mo8Re powder ($FF = 5.4$, i.e., the limited-to-easy powder flowing category).

The flow rate index (*FRI*) measured through the dynamic flow tests is close to unity for both powders (Mo 1.1 and Mo8Re 1.2), meaning that they are insensitive to flow rate variations. A low level of the aeration energy *AE* and the constant pressure drop lead to a similar conclusion about an excellent sphericity of particles of both powders. Slightly larger particles of the alloyed powder (Fig. 2c) result in a lower pressure drop (*PD*) during permeability testing as compared to their pure Mo equivalents. Next, Fig. 4a presents the results of the stability test obtained from the dynamic flow testing mode. Both powders exhibit unstable, but opposite behavior: a decrease in the total energy value observed with the pure Mo powder can be characteristic of deagglomeration, while an increase in this value in the Mo8Re powder can rather be linked to agglomeration, segregation moisture uptake or de-aeration.

Finally, the rheological properties measurements retained to calculate the *AMS* of the two powders are summarized in Table 5 and Fig. 4b shows a radar graph representing all metrics used to calculate the *AMS* value. Since the AMS values of two powders show less than a 6 % difference, they should not manifest any significant differences in terms of their spreading capacities and powder bed densities.

3.2. Density and porosity analyses

Fig. 5 presents the printed density as a function of the h/t ratio. All the process parameters tested led to a density higher than 95 % with a maximum at 98 %. No significant differences were observed between the two tested *VED-BR* sets and a slight increase in density was noticed around $h/t = 3.3$. Based on these results, two parameter sets were retained, the first one leading to the best measured density of the alloyed powder (II-100) and the second set (II-80) having the same density as the highest-density pure molybdenum samples obtained in the previous study, i.e., ~97 %. The latter comparison is intended to isolate the impact of 8 % rhenium addition on the material microstructure from that on the printed density. The binarized images of these two samples are shown in Fig. 5b,c with the related information about pore populations. Note no clear tendency was observed with any of the pore-related metrics with respect to the process parameters. The pores population was evaluated in the [15;45] p/mm^2 range, with a median circularity $C50_p = [0.60;0.75]$ and a median pore size $DE50_p = [35;50]$ µm.

3.3. Crystalline phases and microstructure

XRD analyses (no shown in this paper) were performed on samples just after their printing and only the bcc phase of pure molybdenum was revealed, with no traces of oxidation that may have occurred during the fabrication process. Further analyses were conducted on the polished surface using WDS to gauge the rhenium behavior in the molybdenum matrix and more precisely detect any oxidation signs. As presented in Figure 6abc, the samples are homogeneous, and rhenium did not segregate and was well diffused in the molybdenum matrix. The WDS analyses show an average rhenium content close to the nominal value regardless of the printing parameters used (II-80 Re wt% = 7.8 ± 0.3, II-100 Re wt% = 8.3 ± 0.4). Regarding the residual oxygen content after printing, the IR spectroscopy measurements made on the denser sample (II-100) highlight a significant increase in the oxygen content inside printed parts (875 ± 210 ppm) as compared to the initial proportion inside the spheroidized powder (Table 4). The EBSD analyses were then carried out and the BC maps plotted, with the latter revealing no significant differences between the two samples. They were both relatively

Table 5
Powder rheological characteristics (Hall flow and FT4 rheometer).

Powders	Hall flow	FT4 Rheometer							
	Flowability (s/50 g)	*BD* (g/cm^3)	*CI* (%) at 15 kPa	*PD* (mBar) at 15 kPa	*SE* (mJ/g)	AE_{10} (mJ)	*BFE* (mJ)	*CC* (kPa)	*AMS*
Mo8Re (This study)	38.7 (Blend) 13 (Atom.)	5.16 (±0.99 %)	3.48 (±12.30 %)	2.51 (±14.10 %)	3.35 (±4.24 %)	24.50 (±12.10 %)	1110 (±3.81 %)	1.30	**164**
Mo [57]	< 15*	6.04 (±0.47 %)	7.65 (±6.57 %)	8.31 (±8.51 %)	2.53 (±2.65 %)	10.60 (±6.21 %)	1084 (±1.23 %)	0.33	**159**

* Commercial data.

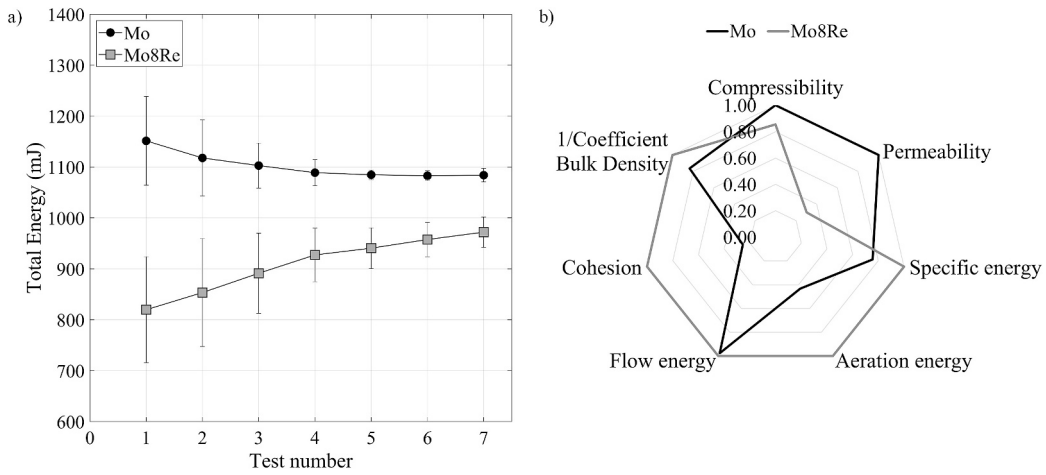

Fig. 4. a) Stability test plots and b) Additive Manufacturing Suitability (*AMS*) radar chart for pure Mo and alloyed Mo8Re powders.

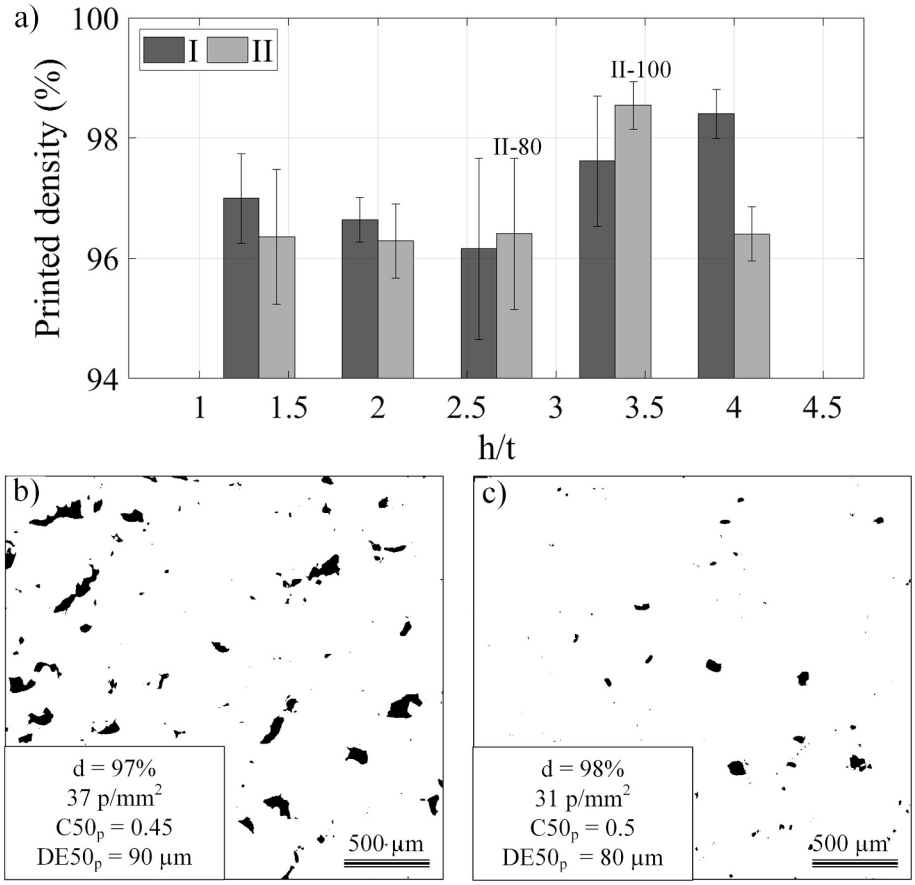

Fig. 5. a) Measured printed densities as functions of the *h*/t ratio for the two *VED-BR* sets; Examples of the binarized surfaces of the samples b) II-80 and c) II-100.

light-colored, which correspond to good quality patterns and indicate that no defects nor internal stresses were detected. Note that in Fig. 6d, one of these maps is presented with a superposed bcc molybdenum phase map (uniformity of color proves a single-phase state of the material). These observations were confirmed by their corresponding statistical distributions (Fig. 6e) which revealed only one peak at BC = 160, suggesting the presence of only one phase associated with molybdenum (Cubic, Im-3 m, 229), which is consistent with the extracted phase map (Fig. 6d), XRD and WDS analyses.

Also from the EBSD analyses, the MacKenzie plots of the misorientation angles (Fig. 7a) were analyzed and associated with those of a conventional polycrystalline cubic material having a random texture [65], which was confirmed by the IPF maps (Fig. 7b) and the pole figures (Fig. 7c). These diagrams also revealed a significant population of structural elements with small misorientation angles (LAGB, $< 10°$), thus reflecting the presence of substructures accommodated by arrays of dislocations. Finally, no significant differences were found in the LAGB and HAGB densities of both Mo8Re samples (Table 6). However, the grain density of the Mo8Re 97 %-density samples was found higher and coinciding with smaller grains and a greater porosity as compared to their Mo8Re 98 %-density equivalents. However, compared to the pure molybdenum samples, the LAGB and HAGB densities of the Mo8Re

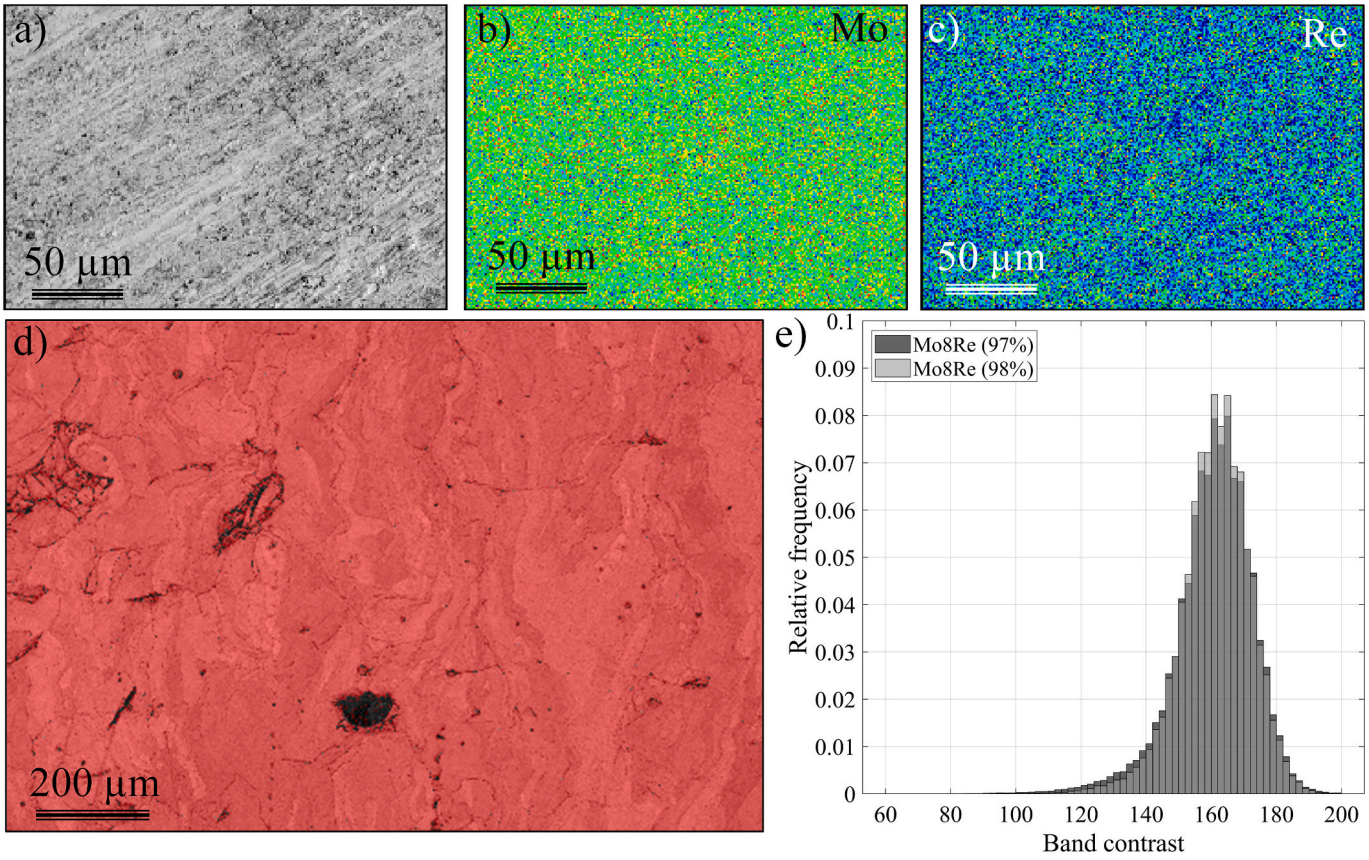

Fig. 6. WDS mapping of the II-100 (98 %) sample: a) polished surface, b) molybdenum and c) rhenium distributions; d) Superposition of the Band Contrast (BC) and bcc molybdenum phase maps of the II-100 (98 %) sample; e) BC cumulative histograms of the two retained samples (II-80 (97 %) and II-100 (98 %)).

samples were 1.5 to 2 times higher, and this increase in boundary densities was accompanied by a 15 to 20 % decrease in the grain size.

3.4. Mechanical testing at room and elevated temperatures

Fig. 8a presents the ultimate compressive strength as a function of the testing temperature for the 97 % and 98 % density Mo8Re samples and their reference 97 %-density pure molybdenum counterparts. At room temperature, both Mo8Re samples show lower strength values than their molybdenum counterparts, and the higher the printed density, the higher the mechanical strength. However, at elevated temperatures, the strength values of two alloyed samples were higher than those of the molybdenum samples. It should be noted that the degree of oxidation of the alloyed and unalloyed samples during testing at elevated temperatures was equivalent, as witnessed by their mass loss (~4 % at 800 °C and ~ 6 % at 1000 °C). Of note, contrary to the 98 %-density Mo8Re samples, 97 %-density Mo8Re samples presented the same non-monotonic temperature evolution of strength as their pure molybdenum counterparts (aging-related increase in strength at around 800 °C [66,67]). This difference in the temperature-related behavior is illustrated by the stress-strain diagrams shown in Fig. 8b,c and comparing the highest-density (98 %) Mo8Re samples with their highest-density (97 %) pure Mo counterparts.

Regarding the strain under maximum load, no significant differences were observed for the alloyed samples when varying the testing temperature, nor between the 98 %-density and the 97 %-density Mo8Re samples. Indeed, as listed in Table 7, the strain under maximum load of the alloyed samples varied from 4 to 7 %, following no particular trend, and representing half that of pure molybdenum. All the mechanical properties (YS, UCS and δ) extracted from these compressive tests, are summarized in Table 7.

3.5. Artifacts

The complex pineapple-shaped structure was successfully printed in two different formats, measuring 4 and 2 cm in height, respectively. The smallest version is not a simple downsizing of the larger one, but rather, a geometric adaptation. Indeed, the leaves in the shorter one are of a shorter stature, with a restricted area allocated to fine letters. However, the lattice strut size of both formats remains almost identical (respectively 680 and 650 µm). No discontinuity was observed at the transition zone between the dense lower part and the lattice structure (Fig. 9a). With regards to the self-supported leave structures (angle = 45°), they were correctly printed throughout their height. On the smaller structure, the text was downsized to fit the available area, and distinguishable fine letters were printed with a minimal thickness going down to 250 µm (Fig. 9b).

4. Discussions

4.1. Printability of the alloyed Mo8Re powder

Among the various prints realized with pure Mo and alloyed Mo8Re powders, a slight difference in terms of spreading behavior was observed. Both powders were found suitable for the LPBF process, exhibiting good flowability and spreading properties that enabled to obtain a highly dense powder bed. However, the alloyed Mo8Re powder appeared to be more sensitive to its environment and prone to agglomeration. Indeed, during printing preparation, it was observed that large agglomerates were formed inside the Mo8Re powder container. They were easily breakable during the powder loading by slight agitation inside the supply chamber and did not impact the quality of the powder spread over the baseplate (Fig. 10a). The agglomerates

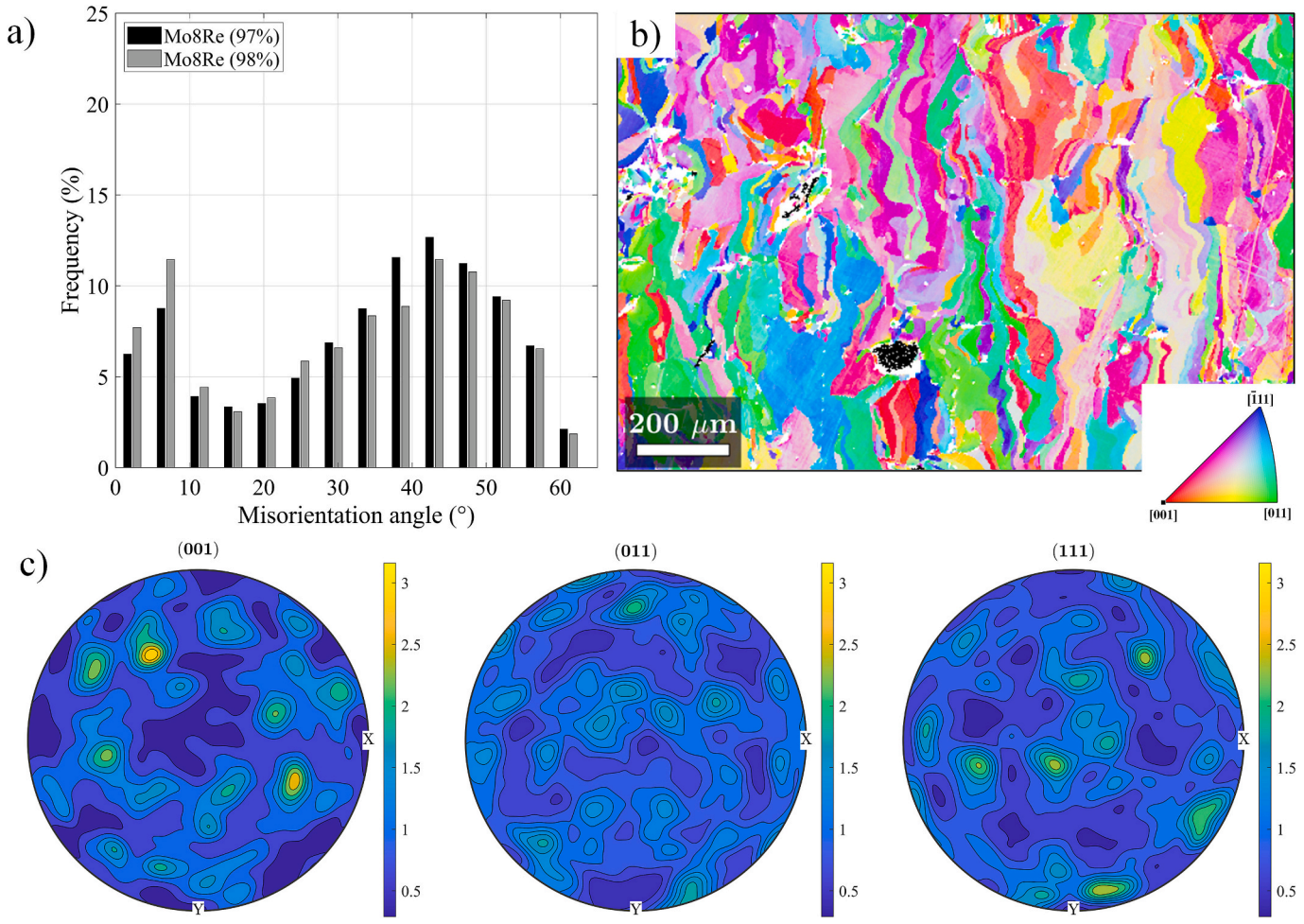

Fig. 7. a) MacKenzie plots of Mo8Re (97 %) and Mo8Re (98 %) samples; b) orientation map (IPF Y) and c) pole figures of a Mo8Re (98 %) sample.

Table 6
Boundary densities, grain density, size and circularity of the two Mo8Re samples retained and the pure molybdenum from the reference work.

Sample	LAGB (μm^{-1})	HAGB (μm^{-1})	Grain density (g/mm^2)	$DE90_g$ (μm)	$C90_g$
Mo8Re (98 %)	0.12	0.062	654	85	0.7
Mo8Re (97 %)	0.10	0.067	804	80	0.65
Mo (97 %)	0.06	0.044	278	100	0.7

were also clearly visible during the unloading of the printer (Fig. 10b). Moreover, blue color traces were observed inside the unsealed containers not used for extended periods of time, evidencing the powder's sensitivity to humidity. This color is correlated with the water dissolution of traces of molybdenum oxide (MoO_3) (Fig. 10c). This sensitivity to humidity and propensity to agglomeration were not observed for pure Mo powders. Overall, the aforementioned printing behavior of the Mo8Re and Mo powders was in agreement with the conclusions of the rheological measurements (*CC*, *AE*) described in Section 3.1.2.

4.2. Impact of the 8 wt% rhenium addition on the printed density and chemistry

It was observed in this work that adding 8 wt% of rhenium increased the overall density of printed parts (Fig. 5) as compared to those of pure molybdenum [57]. Indeed, for the same combinations of process parameters, the printed density range of the Mo8Re parts (96–98 %) is higher and narrower than that of the pure Mo parts (89–97 %). Since it is a known fact that the rhenium addition [68], even in small proportions [69], enables to decrease the DBTT, and therefore increase the ductility of refractory metals, it may be hypothesized that this phenomenon was one of the main contributing factors to the enhanced densification during printing.

As far as the Re content is concerned, the literature highlighted the metastability of brittle phases in Mo—Re alloys (σ [70] or χ), especially for high rhenium contents and processes involving high cooling rates [71]. Consequently, the production of high rhenium-containing powders and the use of these powders for 3D printing could be challenging as both processes, plasma atomization and LPBF, involve high cooling rates. In our study, a relatively small rhenium addition was homogeneously accommodated inside the bcc crystallographic structure of molybdenum, in agreement with the Mo—Re phase diagram [64]. This excellent solid solubility of Re in Mo led to a final chemical composition close to the nominal value (≈ 8 wt%) regardless of the printing parameters (see Section 3.3).

It is reasonable to assert that even higher printed densities can be obtained provided both the Re content and the LPBF conditions are optimized. However, the amount of data on the additive manufacturing of Mo—Re alloys actually available is insufficient to allow to propose an optimal rhenium content for these compounds. This is especially true because of the multitude of factors impacting the densification behavior and the cracking susceptibility of refractory alloys during their laser powder bed fusion.

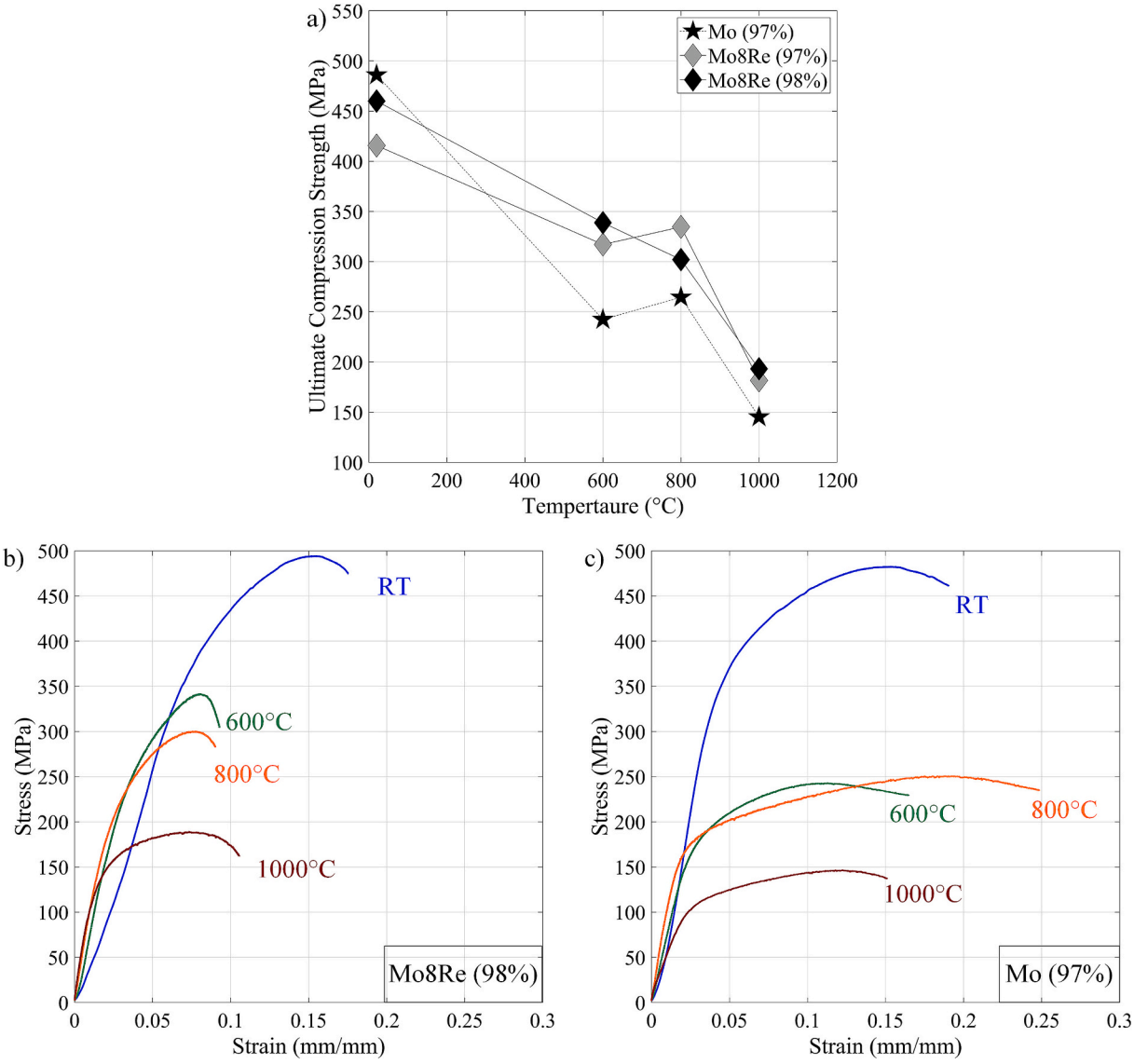

Fig. 8. a) Evolution of the Ultimate Compression Strength as a function of the testing temperature; b) Typical stress-strain curves at all tested temperatures for b) Mo8Re (98 %) and c) Mo (97 %) samples.

Table 7
Mechanical properties in compression at room and elevated temperatures.

Sample	Temperature (°C)	YS (MPa)	UCS (MPa)	δ (%)
Mo8Re (98 %)	20	303 ± 30	460 ± 31	7 ± 1.3
	600	206 ± 8	339 ± 1	4 ± 0.5
	800	186 ± 10	302 ± 20	4 ± 0.3
	1000	119 ± 28	193 ± 31	6 ± 0.6
Mo8Re (97 %)	20	256 ± 2	416 ± 22	7 ± 0.8
	600	205 ± 28	317 ± 19	4 ± 1.2
	800	206 ± 8	335 ± 6	4 ± 0.6
	1000	119 ± 4	182 ± 11	6 ± 0.1
Mo (97 %)	20	340 ± 20	500 ± 15	11 ± 1
	600	150 ± 20	240 ± 30	8 ± 1
	800	160 ± 5	260 ± 8	14 ± 1
	1000	90 ± 10	150 ± 18	9 ± 4

4.3. Microstructure

In conventional powder metallurgy, it was observed that a rhenium addition contributes to a refinement of the microstructure and increases the recrystallization temperature of refractory alloys. In fact, a NASA technical report [69] showed that for the same manufacturing and post-treatment conditions, Mo—14Re (wt%) parts exhibited a finer microstructure than their pure molybdenum equivalents. Similar observations related to rhenium alloying have also been reported for LPBF Mo—Re alloys with respect to the grain refinement [39] and texture evolution [26]. However, these effects have thus far only been reported for samples printed using rhenium contents greater than 25 wt%.

When comparing the microstructure of the Mo8Re (actual work) and Mo [57] samples printed using the same sets of printing parameters (II-80 or II-100 in Table 3, $P = 180$ W, $v = 188$ or 150 mm/s, $h = 80$ or 100 µm, $t = 30$ µm), it can be concluded that even a relatively small addition of rhenium, such as that in this study (8 wt%), also results in microstructure refinement: (II-80: 105 µm (Mo) to 80 µm (Mo8Re) and II-100: 125 µm (Mo) to 85 µm (Mo8Re). For the other microstructural features, neither the columnar aspect nor the texture, seem to be affected by adding rhenium, regardless of the printing parameters used.

4.4. Mechanical properties

Alloying of Mo with Re has been proven efficient in strongly increasing the mechanical properties at room temperature, as

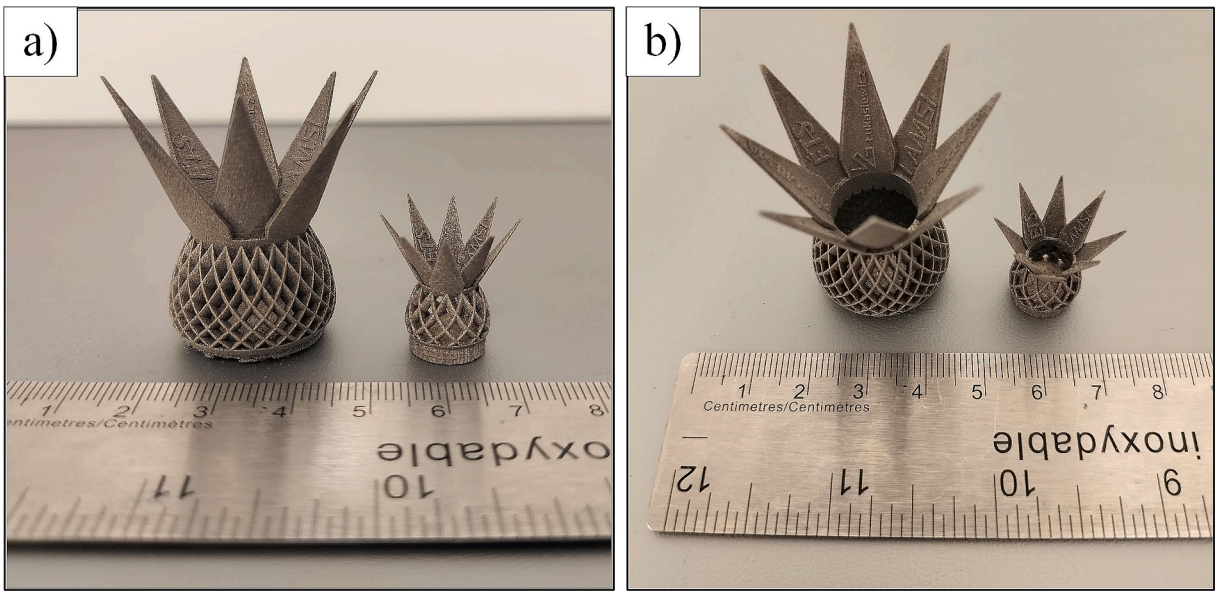

Fig. 9. a) Side view and b) inclined view of the pineapple artifacts printed using Mo8Re powder.

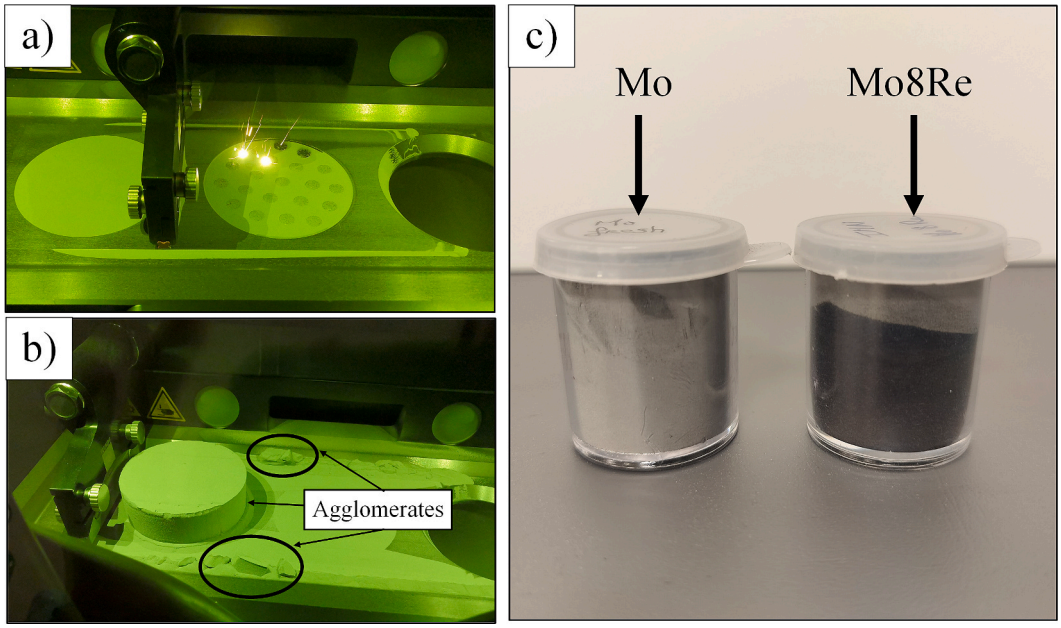

Fig. 10. a) Powder bed of Mo8Re during printing. b) Agglomerates of Mo8Re powders observed during the printer unloading. c) Unsealed containers for storing samplings of pure Mo and alloyed Mo8Re powders. A dark blue color observed on the surface of Mo8Re is correlated with that of molybdenum oxides dissolution in water. (For interpretation of the references to color in this figure legend, the reader is referred to the web version of this article.)

demonstrated by compression testing of Mo-47.5wt%Re LPBF samples in [26]. An enhancement of the mechanical strength of alloyed LPBF parts as compared to their pure molybdenum equivalents has also been highlighted by flexural testing of MoRe samples with rhenium contents of 10 and 25 wt% [39]. In the latter study, parts with a lower rhenium concentration (5 wt%) were also tested, but showed lower mechanical properties at room temperature than their pure Mo counterparts. These findings align with the observations of the present study and can be attributed to the rhenium softening effect in MoRe alloys with lower Re contents described in [40]. Note that this softening effect in Mo-low Re content alloy specimens processed by powder sintering and hot radial forging was observed in their as-worked conditions only [72]. Heat treatments, such as stress relief and recrystallization annealing, led to microstructural changes (dislocation density reduction, grain coarsening, etc.), which suppressed the softening effect. A dedicated study on the impact of heat treatments of LPBF-processed molybdenum-rhenium specimens with low rhenium content on their mechanical properties is yet to be conducted.

To the best of the authors' knowledge, the effect of rhenium addition on the mechanical properties of additively manufactured molybdenum parts at elevated temperatures is yet to be addressed. However, the literature attests that the addition of rhenium, even in small proportions, improves the mechanical properties of conventionally-manufactured molybdenum parts. For example, [69], a progressive increase in rhenium content (from 7 to 14 at.%) enabled to increase the ultimate strength of hot isostatic pressed (HIP-ed) tensile specimens in the 980 to 1650 °C temperature range (almost a twofold increase for 14at% Re addition). A more recent study on powder metallurgy processed Mo42.5

wt% Re parts [73] also showed a significant increase in the mechanical properties at temperatures of up to 1200 °C. These observations are in line with those of this study, indicating an increase in the elevated temperature properties of MoRe alloys as compared to their Mo equivalents.

5. Conclusions

In this study, the spheroidization process was used to change the shape of particles from agglomerated granules to a powder with good particles sphericity and rheological properties suitable for the LPBF process. It also reduced the specific surface area (BET) of the powders by 80 %, but according to pycnometric measurements, had no effect on the powder density. The chemical composition within individual particles was homogenized to an average of 8 % wt% of rhenium and was preserved and homogenously distributed in the molybdenum matrix after printing. The selected optimal set of printing parameters ($P = 180$ W, $v = 188$ mm/s, $h = 100$ µm and $t = 30$ µm) led to the printing of crack-free specimens with a density of 98 %. Adding rhenium caused a decrease in both the compression strength and strain under maximum load at room temperature as compared to samples printed with pure Mo powders. However, it led to significantly higher mechanical properties in the 600–1000 °C temperature range (ultimate strength of 340 and 190 MPa at 600 and 1000 °C, respectively). Finally, fine letter- and lattice-containing complex structures were successfully printed to demonstrate the printability of these powders.

CRediT authorship contribution statement

Aurore Leclercq: Writing – original draft, Visualization, Software, Methodology, Investigation, Formal analysis, Data curation, Conceptualization. **Anna Czech:** Writing – original draft, Visualization, Investigation, Data curation. **Thibault Mouret:** Writing – original draft, Visualization, Software, Methodology, Investigation, Formal analysis, Data curation. **Marcin Lis:** Writing – original draft, Investigation, Data curation. **Adriana Wrona:** Supervision, Resources, Methodology. **Vladimir Brailovski:** Writing – review & editing, Visualization, Validation, Supervision, Resources, Project administration, Methodology, Funding acquisition, Conceptualization.

Declaration of competing interest

The authors declare that they have no known competing financial interests or personal relationships that could have appeared to influence the work reported in this paper.

Acknowledgments

The authors acknowledge the financial support provided by PRIMA Québec (Pôle de recherche et d'innovation en matériaux avancés) in the framework of the M-ERA.NET program, NSERC (Natural Sciences and Engineering Research Council of Canada) and PyroGenesis Canada Inc.

Data availability

Data are contained within the article.

References

[1] R.A. Holmwood, R. Glang, Resistivity and temperature coefficient of pure molybdenum, J. Chem. Eng. Data 10 (2) (1965) 162–163, https://doi.org/10.1021/je60025a028.
[2] P. Rebesan, et al., Pure molybdenum manufactured by laser powder bed fusion: thermal and mechanical characterization at room and high temperature, Addit. Manuf. 47 (2021) 102277, https://doi.org/10.1016/j.addma.2021.102277.
[3] P. Hidnert, W.B. Gero, Thermal expansion of molybdenum, Sci. Pap. Bur. Stand. 19 (1924) 429, https://doi.org/10.6028/nbsscipaper.171.
[4] H. Baker, Properties of metals, in: J.R. Davis (Ed.), Metals Handbook Desk Edition, 2nd ed, ASM International, 1998, pp. 114–121, https://doi.org/10.31399/asm.hb.mhde2.a0003086.
[5] Y.-J. Hwang, Y. Kim, S.-H. Park, S.-C. Park, K.-A. Lee, Wear and corrosion properties of pure Mo coating layer manufactured by atmospheric plasma spray process, Arch. Metall. Mater. (2024) 81–85, https://doi.org/10.24425/amm.2024.147790.
[6] H. Zhao, L. Xie, C. Xin, N. Li, B. Zhao, L. Li, Effect of molybdenum content on corrosion resistance and corrosion behavior of Ti-Mo titanium alloy in hydrochloric acid, Mater. Today Commun. 34 (2023) 105032, https://doi.org/10.1016/j.mtcomm.2022.105032.
[7] Plansee, Des Métaux Solides Pour des Produits Solides | Plansee [Online]. Available, https://www.plansee.com/www.plansee.com/fr.html, 2023.
[8] J. Wadsworth, T.G. Nieh, J.J. Stephens, Recent advances in aerospace refractory metal alloys, Int. Mater. Rev. 33 (1) (1988) 131–150, https://doi.org/10.1179/imr.1988.33.1.131.
[9] J.A. Shields Jr., Applications of Molybdenum Metal and Its Alloys, International Molybdenum Association, 2013.
[10] D. Wang, C. Yu, J. Ma, W. Liu, Z. Shen, Densification and crack suppression in selective laser melting of pure molybdenum, Mater. Des. 129 (2017) 44–52, https://doi.org/10.1016/j.matdes.2017.04.094.
[11] A. Talignani, et al., A review on additive manufacturing of refractory tungsten and tungsten alloys, Addit. Manuf. 58 (2022) 103009, https://doi.org/10.1016/j.addma.2022.103009.
[12] A. Garcia-Colomo, D. Wood, F. Martina, S.W. Williams, A comparison framework to support the selection of the best additive manufacturing process for specific aerospace applications, Int. J. Rapid Manuf. 9 (2–3) (2020) 194–211, https://doi.org/10.1504/IJRAPIDM.2020.107736.
[13] P. Gradl, et al., Robust metal additive manufacturing process selection and development for aerospace components, J. Mater. Eng. Perform. 31 (8) (2022) 6013–6044, https://doi.org/10.1007/s11665-022-06850-0.
[14] E. Pink, R.W. Armstrong, Total Material Variables Influencing DBTT for Molybdenum, Technical Report to Office Of Naval Research NR031–739 Vol. I, 1970. Accessed: Jul. 22, 2024[Online]. Available, https://apps.dtic.mil/sti/pdfs/AD0713191.pdf.
[15] Y. Hiraoka, Significant effect of carbon content in the low-temperature fracture behavior of molybdenum, Mater. Trans. JIM 31 (10) (1990) 861–864, https://doi.org/10.2320/matertrans1989.31.861.
[16] Y. Hiraoka, H. Kurishita, M. Narui, H. Kayano, Fracture and ductile-to-brittle transition characteristics of molybdenum by impact and static bend tests, Mater. Trans. JIM 36 (4) (1995) 504–510, https://doi.org/10.2320/matertrans1989.36.504.
[17] H. Xing, et al., Effects of oxygen on microstructure and evolution mechanism of body-centred-cubic molybdenum, Int. J. Refract. Met. Hard Mater. 103 (2022) 105747, https://doi.org/10.1016/j.ijrmhm.2021.105747.
[18] A. Iveković, et al., Selective laser melting of tungsten and tungsten alloys, Int. J. Refract. Met. Hard Mater. 72 (2018) 27–32, https://doi.org/10.1016/j.ijrmhm.2017.12.005.
[19] J. Braun, et al., Molybdenum and tungsten manufactured by selective laser melting: analysis of defect structure and solidification mechanisms, Int. J. Refract. Met. Hard Mater. 84 (2019) 104999, https://doi.org/10.1016/j.ijrmhm.2019.104999.
[20] A.V. Müller, et al., Additive manufacturing of pure tungsten by means of selective laser beam melting with substrate preheating temperatures up to 1000 °C, Nucl. Mater. Energy 19 (2019) 184–188, https://doi.org/10.1016/j.nme.2019.02.034.
[21] N. Alinejadian, P. Wang, L. Kollo, K.G. Prashanth, Selective laser melting of commercially pure molybdenum by laser rescanning, 3D Print Addit. Manuf. 10 (4) (2023) 785–791, https://doi.org/10.1089/3dp.2021.0265.
[22] B. Guan, et al., Strategies to reduce pores and cracks of molybdenum fabricated by selective laser melting, Int. J. Refract. Met. Hard Mater. 112 (2023) 106123, https://doi.org/10.1016/j.ijrmhm.2023.106123.
[23] L. Kaserer, et al., Fully dense and crack free molybdenum manufactured by selective laser melting through alloying with carbon, Int. J. Refract. Met. Hard Mater. 84 (2019) 105000, https://doi.org/10.1016/j.ijrmhm.2019.105000.
[24] N.E. Ellsworth, et al., Influence of Nano-sized SiC on the laser powder bed fusion of molybdenum, Crystals 12 (2022), https://doi.org/10.3390/cryst12091276.
[25] J. Gan, et al., Research about the microcrack mechanisms in molybdenum and corresponding suppression strategies during laser additive manufacturing process, Materialia 36 (2024) 102173, https://doi.org/10.1016/j.mtla.2024.102173.
[26] F. Oehlerking, M.T. Stawovy, S. Ohm, A. Imandoust, Microstructural characterization and mechanical properties of additively manufactured molybdenum and molybdenum alloys, Int. J. Refract. Met. Hard Mater. 109 (2022) 105971, https://doi.org/10.1016/j.ijrmhm.2022.105971.
[27] D. Wang, Z. Wang, K. Li, J. Ma, W. Liu, Z. Shen, Cracking in laser additively manufactured W: initiation mechanism and a suppression approach by alloying, Mater. Des. 162 (2019) 384–393, https://doi.org/10.1016/j.matdes.2018.12.010.
[28] M. Guo, K. Liu, J. Sun, D. Gu, Laser powder bed fusion of a novel nano-modified tungsten alloy with refined microstructure and enhanced strength, Mater. Sci. Eng. A 843 (2022) 143096, https://doi.org/10.1016/j.msea.2022.143096.
[29] T. Takida, H. Kurishita, M. Mabuchi, T. Igarashi, Y. Doi, T. Nagae, Mechanical properties of fine-grained, sintered molybdenum alloys with dispersed particles developed by mechanical alloying, Mater. Trans. 45 (1) (2004) 143–148, https://doi.org/10.2320/matertrans.45.143.
[30] P. Hu, et al., Preparation and ductile-to-brittle transition temperature of the La-TZM alloy plates, Int. J. Refract. Met. Hard Mater. 52 (2015) 131–136, https://doi.org/10.1016/j.ijrmhm.2015.05.006.

[31] J. Xu, et al., Enhanced strength and ductility of laser powder bed fused NbMoTaW refractory high-entropy alloy via carbon microalloying, Addit. Manuf. Lett. 3 (2022) 100079, https://doi.org/10.1016/j.addlet.2022.100079.
[32] T. Ron, et al., Synthesis of refractory high-entropy alloy WTaMoNbV by powder bed fusion process using mixed elemental alloying powder, Materials 15 (2022), https://doi.org/10.3390/ma15124043.
[33] L. Kaserer, et al., Microstructure and mechanical properties of molybdenum-titanium-zirconium-carbon alloy TZM processed via laser powder-bed fusion, Int. J. Refract. Met. Hard Mater. 93 (2020) 105369, https://doi.org/10.1016/j.ijrmhm.2020.105369.
[34] L. Kaserer, et al., Molybdenum alloy Mo-Ti-Zr-C adapted for laser powder bed fusion with refined isotropic microstructure and excellent high temperature strength, Int. J. Refract. Met. Hard Mater. 113 (2023) 106174, https://doi.org/10.1016/j.ijrmhm.2023.106174.
[35] T. Leonhardt, J.-C. Carlén, M. Buck, C.R. Brinkman, W. Ren, C.O. Stevens, Investigation of mechanical properties and microstructure of various molybdenum-rhenium alloys, AIP Conf. Proc. 458 (1) (1999) 685–690, https://doi.org/10.1063/1.57638.
[36] T. Yamamoto, M. Hara, Y. Hatano, Cracking behavior and microstructural, mechanical and thermal characteristics of tungsten–rhenium binary alloys fabricated by laser powder bed fusion, Int. J. Refract. Met. Hard Mater. 100 (2021) 105651, https://doi.org/10.1016/j.ijrmhm.2021.105651.
[37] J. Li, Y. Wu, L. Xue, Z. Wei, Laser powder bed fusion in-situ alloying of refractory WTa alloy and its microstructure and mechanical properties, Addit. Manuf. 67 (2023) 103493, https://doi.org/10.1016/j.addma.2023.103493.
[38] R.H. Cooper Jr., E.E. Hoffman, Refractory Alloy Technology for Space Nuclear Power Applications, Oak Ridge National Laboratory and U.S Department of Energy oak Ridge Operations, Oak Ridge, Tennessee, USA, 1984. CONF-8308130; ON: DE84001745.
[39] C.C. Eckley, et al., Evaluating molybdenum-rhenium alloys through additive manufacturing, JOM 75 (6) (2023) 1928–1940, https://doi.org/10.1007/s11837-023-05813-7.
[40] J.R. Stephens, W.R. Witzke, Alloy softening in group via metals alloyed with rhenium, J. Common Met. 23 (4) (1971) 325–342, https://doi.org/10.1016/0022-5088(71)90043-9.
[41] N.R. Philips, M. Carl, N.J. Cunningham, New opportunities in refractory alloys, Metall. Mater. Trans. A 51 (7) (2020) 3299–3310, https://doi.org/10.1007/s11661-020-05803-3.
[42] A.C. Field, L.N. Carter, N.J.E. Adkins, M.M. Attallah, M.J. Gorley, M. Strangwood, The effect of powder characteristics on build quality of high-purity tungsten produced via laser powder bed fusion (LPBF), Metall. Mater. Trans. A 51 (3) (2020) 1367–1378, https://doi.org/10.1007/s11661-019-05601-6.
[43] X. Liu, K. Wang, P. Hu, Q. Chen, A.A. Volinsky, Spheroidization of molybdenum powder by radio frequency thermal plasma, Int. J. Miner. Metall. Mater. 22 (11) (2015) 1212–1218, https://doi.org/10.1007/s12613-015-1187-7.
[44] Z. Hao, et al., Spheroidization of a granulated molybdenum powder by radio frequency inductively coupled plasma, Int. J. Refract. Met. Hard Mater. 82 (2019) 15–22, https://doi.org/10.1016/j.ijrmhm.2019.03.023.
[45] S. Qiu, B.K. Chen, C.S. Xiang, Preparation and properties of spherical Mo powders by plasma rotating electrode process for additive manufacturing, Mater. Sci. Forum 993 (2020) 391–397, https://doi.org/10.4028/www.scientific.net/MSF.993.391.
[46] F. Hinrichs, et al., Flexible powder production for additive manufacturing of refractory metal-based alloys, Metals 11 (2021), https://doi.org/10.3390/met11111723.
[47] B. Bałasz, M. Bielecki, W. Gulbiński, Ł. Słoboda, Comparison of ultrasonic and other atomization methods in metal powder production, J. Achiev. Mater. Manuf. Eng. 116 (1) (2023) 11–24, https://doi.org/10.5604/01.3001.0016.3393.
[48] T. Fedina, J. Sundqvist, J. Powell, A.F.H. Kaplan, A comparative study of water and gas atomized low alloy steel powders for additive manufacturing, Addit. Manuf. 36 (2020) 101675, https://doi.org/10.1016/j.addma.2020.101675.
[49] K. Kassym, A. Perveen, Atomization processes of metal powders for 3D printing, Mater. Today Proc. 26 (2020) 1727–1733, https://doi.org/10.1016/j.matpr.2020.02.364.
[50] S.Z. Soong, W.L. Lai, A.N. Kay Lup, Atomization of metal and alloy powders: processes, parameters, and properties, AICHE J. 69 (11) (2023) e18217, https://doi.org/10.1002/aic.18217.
[51] T. Majewski, Research of Spheroidization processes of W-re powders, Solid State Phenom. 199 (2013) 490–495, https://doi.org/10.4028/www.scientific.net/SSP.199.490.
[52] A. Wrona, et al., Ni–Cr powders modified with rhenium as a novel coating material—physical properties, microstructure, and behavior in plasma plume, Materials 15 (2022), https://doi.org/10.3390/ma15113844.
[53] J. Tang, et al., Reaction mechanism and process control of hydrogen reduction of ammonium Perrhenate, Metals 10 (2020), https://doi.org/10.3390/met10050640.
[54] F.R. Caliari, F.S. Miranda, D.A.P. Reis, G.P. Filho, L.I. Charakhovski, A. Essiptchouk, Plasma torch for supersonic plasma spray at atmospheric pressure, J. Mater. Process. Technol. 237 (2016) 351–360, https://doi.org/10.1016/j.jmatprotec.2016.06.027.
[55] R. Freeman, Measuring the flow properties of consolidated, conditioned and aerated powders — a comparative study using a powder rheometer and a rotational shear cell, Powder Technol. 174 (1) (2007) 25–33, https://doi.org/10.1016/j.powtec.2006.10.016.
[56] R. Freeman, X. Fu, Characterisation of powder bulk, dynamic flow and shear properties in relation to die filling, Powder Metall. 51 (3) (2008) 196–201, https://doi.org/10.1179/174329008X324115.
[57] A. Leclercq, T. Mouret, V. Brailovski, Laser powder bed fusion of molybdenum: density, structure and mechanical properties at room and elevated temperatures, Mater. Sci. Eng. A (2025) 148004, https://doi.org/10.1016/j.msea.2025.148004.
[58] S.E. Brika, M. Letenneur, C.A. Dion, V. Brailovski, Influence of particle morphology and size distribution on the powder flowability and laser powder bed fusion manufacturability of Ti-6Al-4V alloy, Addit. Manuf. 31 (2020) 100929, https://doi.org/10.1016/j.addma.2019.100929.
[59] C. Tan, K. Zhou, W. Ma, B. Attard, P. Zhang, T. Kuang, Selective laser melting of high-performance pure tungsten: parameter design, densification behavior and mechanical properties, Sci. Technol. Adv. Mater. 19 (1) (2018) 370–380, https://doi.org/10.1080/14686996.2018.1455154.
[60] A. Leclercq, V. Brailovski, Improving laser powder bed fusion printability of tungsten powders using simulation-driven process optimization algorithms, Materials 17 (2024), https://doi.org/10.3390/ma17081865.
[61] E04 Committee, Practice for Determining Average Grain Size Using Electron Backscatter Diffraction (EBSD) in Fully Recrystallized Polycrystalline Materials, E2627, 2025, https://doi.org/10.1520/E2627-13R19.
[62] Test Methods of Compression Testing of Metallic Materials at Room Temperature, E9–09, 2025, https://doi.org/10.1520/E0009-09.
[63] E28 Committee, Practice for Compression Tests of Metallic Materials at Elevated Temperatures With Conventional or Rapid Heating Rates and Strain Rates, 2025, https://doi.org/10.1520/E0209-18.
[64] H. Okamoto, Mo-Re (Molybdenum-Rhenium), J. Phase Equilib. Diffus. 31 (6) (2010) 580–581, https://doi.org/10.1007/s11669-010-9787-4.
[65] J.K. Mason, C.A. Schuh, The generalized Mackenzie distribution: disorientation angle distributions for arbitrary textures, Acta Mater. 57 (14) (2009) 4186–4197, https://doi.org/10.1016/j.actamat.2009.05.016.
[66] R.P. Carreker, R.W. Guard, Tensile deformation of molybdenum as a function of temperature and strain rate, JOM 8 (2) (1956) 178–184, https://doi.org/10.1007/BF03377669.
[67] A.H. Cottrell, B.A. Bilby, Dislocation theory of yielding and strain ageing of Iron, Proc. Phys. Soc. Sect. A 62 (1) (1949) 49–62, https://doi.org/10.1088/0370-1298/62/1/308.
[68] W.D. Klopp, Review of Ductilizing of Group via Elements by Rhenium and Other Solutes, National Aeronautics and Space Administration, Cleveland, OH (USA), 1968. Lewis Research Center, Technical Note NASA-TN-D-4955. Accessed: Nov. 22, 2024. [Online]. Available, https://www.osti.gov/biblio/5785668.
[69] W.D. Klopp, W.R. Witzke, Mechanical Properties of Electron-Beam-Melted Molybdenum and Dilute Molybdenum-Rhenium Alloys, NASA Lewis Research Center, Cleveland, OH, USA, Technical Memorandum NASA-TM-X-2576, 1972. Accessed: Nov. 22, 2024. [Online]. Available, https://ntrs.nasa.gov/citations/19720017873.
[70] J.-C. Carlen, B.D. Bryskin, Concerning sigma-phase in molybdenum-rhenium alloys, J. Mater. Eng. Perform. 3 (2) (1994) 282–291, https://doi.org/10.1007/BF02645854.
[71] R.L. Mannheim, J.L. Garin, Structural identification of phases in Mo–re alloys within the range from 5 to 95% re, J. Mater. Process. Technol. 143–144 (2003) 533–538, https://doi.org/10.1016/S0924-0136(03)00342-X.
[72] G. Leichtfried, J.H. Schneibel, M. Heilmaier, Ductility and impact resistance of powder-metallurgical molybdenum-rhenium alloys, Metall. Mater. Trans. A 37 (10) (2006) 2955–2961, https://doi.org/10.1007/s11661-006-0177-9.
[73] H. Huang, et al., Hot compression behaviors and microstructural evolution of Mo-42 wt%re alloy, Mater. Lett. 318 (2022) 132252, https://doi.org/10.1016/j.matlet.2022.132252.